Point Set Registration Using Havrda–Charvat–Tsallis Entropy Measures

Nicholas J. Tustison*, Suyash P. Awate, Gang Song, Tessa S. Cook, and James C. Gee

***Abstract*—We introduce a labeled point set registration algorithm based on a family of novel information-theoretic measures derived as a generalization of the well-known Shannon entropy. This generalization, known as the Havrda–Charvat–Tsallis entropy, permits a fine-tuning between solution types of varying degrees of robustness of the divergence measure between multiple point sets. A variant of the traditional free-form deformation approach, known as *directly manipulated free-form deformation*, is used to model the transformation of the registration solution. We provide an overview of its open source implementation based on the Insight Toolkit of the National Institutes of Health. Characterization of the proposed framework includes comparison with other state of the art kernel-based methods and demonstration of its utility for lung registration via labeled point set representation of lung anatomy.**

***Index Terms*—Directly manipulated free-form deformation, Jensen–Havrda–Charvat–Tsallis, lung registration, manifold Parzen windowing, point set registration.**

I. Introduction

POINT set registration is an important element in many medical image analysis solutions which aim to establish geometric correspondences between structures represented as point sets. Early seminal research in point set matching includes the iterative closest point (ICP) algorithm of Besl and McKay [1]. Nearest neighbors are matched between fixed and moving point sets. The optimal transformation parameters are subsequently generated from the matching process which are then used to warp the moving point set. This iterative procedure cycles until convergence. Subsequent extension proposals sought to improve various aspects of the algorithm from tailored optimization strategies [2] to varying the geometric entities of interest [3]. A formal classification of such improvements is provided in [2]. Rangarajan *et al.* formulate a related algorithm known as "softassign" which relaxes the exact correspondence problem [4]. Extensions to this work include that of [5] and [6].

Manuscript received August 13, 2010; revised October 01, 2010; accepted October 04, 2010. Date of publication October 11, 2010; date of current version February 02, 2011. *Asterisk indicates corresponding author.*

*N. J. Tustison is with the University of Virginia, Radiology, Charlottesville, VA 22903 USA (e-mail: ntustison@virginia.edu).

S. P. Awate is with the Scientific Computing and Imaging (SCI) Institute, University of Utah, Salt Lake City, UT 84112 USA (e-mail: suyash@cs.utah.edu).

G. Song, T. S. Cook, and J. C. Gee are with the Department of Radiology, University of Pennsylvania, Philadelphia, PA 19104 USA (e-mail: songgang@seas.upenn.edu; tessa@alumni.upenn.edu; james.gee@uphs.upenn.edu).

Color versions of one or more of the figures in this paper are available online at http://ieeexplore.ieee.org.

Digital Object Identifier 10.1109/TMI.2010.2086065

Other foundational research in point set registration encompasses the exact landmark matching methodology of Bookstein [7] who used thin-plate splines to define the spatial transformation between corresponding sets of landmarks. Rohr *et al.* continued this development in designing *approximating* thin-plate splines [8] which relax the exact correspondence constraint. Joshi and Miller introduced the landmark matching problem to a transformation space defined by diffeomorphisms for large, topologically consistent deformations [9].

More recent work has drawn upon the rich information-theoretic research literature for inspiration of new metrics for point set correspondence. Tsin and Kanade use a kernel density estimation scheme for approximating a smoothed probability density function (PDF) from a point set [10]. Correspondence with other similarly constructed PDFs are assessed utilizing correlation. Independently formulated yet employing a similar strategy, Singh et al., dub their correspondence measure *kernel density correlation* [11].

In order to mitigate the effects of outlier and noise over previous approaches, Jian and Vemuri formulate an L_2 distance between two PDFs generated from distinct point sets using nonparametric density estimation with Gaussian kernels [12]. As an interesting theoretical contribution, they elicit the connection between their L_2 distance and ML-based estimation not only for a pair of PDFs but for multiple PDFs as well. Such investigation draws interesting relationships to an actual distance metric. An L_2 distance is also used by Guo *et al.* who match point sets in the space of diffeomorphisms [13].

Wang *et al.* generalize the Kullback-Leibler (KL) divergence measure to the Jensen-Shannon (JS) divergence measure for point set registration [14]. They couple the JS divergence for point sets with a thin-plate transformation model for the construction of unbiased atlases. Not only does this generalization accommodate the unbiased registration of multiple point sets but several interesting properties of the Jensen-Shannon measure make it viable for paired point set registration. Recent extension of their work includes a generalization of the JS divergence measure [15]. This so-called *Generalized L2-divergence* is also used to construct unbiased shape templates.

Also related to our research is the work of Basu *et al.* who propose a class of estimators between pairs of PDFs, known as the *density power divergence* (DPD), which is characterized by a single, tunable parameter, $\phi \in [0, 1]$ [16]. The authors demonstrate that at the lower extreme, i.e., $\phi = 0$, the DPD reduces to the KL divergence whereas at the upper extreme, i.e., $\phi = 1$, the DPD is equivalent to the L_2 measure between the two PDFs thus allowing a control mechanism for tuning between these two types of solutions. Further discussion is provided in [17].

In this paper we detail the following contributions. 1) We propose a novel point set similarity measure based on the Havrda–Charvat–Tsallis entropy which has a tuneable parameter for controlling the type of solution obtained (Section II). 2) Manifold Parzen windowing is used for assessing the local point set structure (Section II-C). 3) Source code, including testing and documentation, is provided as open source based on the Insight Toolkit (Section IV). 4) We also perform an extensive performance evaluation including comparison with previous kernel-based methods (Section V). We point out that preliminary work was discussed in [18] which has been significantly revised and expanded in this work including the extensive evaluation section.

II. Jensen–Havrda–Charvat–Tsallis Divergence Measure

A. Overview

For a random variable $X : \Omega \mapsto \Re^D$, on sample space Ω, taking N values $x \in \Re^D$ and with PDF $\mathbf{P}(X)$, the well-known Shannon entropy is defined as follows [19]:

$$H(\mathbf{P}(X)) = -\int_{\Re^D} \mathbf{P}(x)\log\mathbf{P}(x)dx \approx -\frac{1}{N}\sum_{x\sim\mathbf{P}(X)} \log\mathbf{P}(x) \quad (1)$$

where $x \sim \mathbf{P}(X)$ denotes that x is randomly drawn from the PDF $\mathbf{P}(X)$—a step directly justified by the weak law of large numbers [20]. An extension of the Shannon entropy, the Havrda–Charvat–Tsallis (HCT) entropy, was introduced in [21] and further developed in [22], [23]. It is parameterized by a variable, $\alpha > 0$, such that the HCT entropy [19] is defined to be

$$H_\alpha(\mathbf{P}(X)) = \frac{1}{1-\alpha}\left[\int_{\Re^D}[\mathbf{P}(x)]^\alpha dx - 1\right] \approx \frac{1}{1-\alpha}\left[\frac{1}{N}\sum_{x\sim\mathbf{P}(X)}[\mathbf{P}(x)]^{\alpha-1} - 1\right]. \quad (2)$$

It is well known that $H_\alpha(\cdot)$ reduces to the conventional Shannon entropy as $\alpha \to 1$ [19], [23].

Similar to the Jensen–Shannon (JS) divergence, given the HCT entropy, one can define a generalized mutual information measure for a set of random variables. This measure is known as the Jensen–Havrda–Charvat–Tsallis (JHCT) divergence [19] and is calculated from K PDFs as follows:

$$\mathrm{JHCT}_\alpha(\mathbf{P}_1(X_1),\ldots,\mathbf{P}_K(X_K),\gamma_1,\ldots,\gamma_K) = H_\alpha\left(\sum_{k=1}^K \gamma_k\mathbf{P}_k(X_k)\right) - \sum_{k=1}^K \gamma_k H_\alpha\left(\mathbf{P}_k(X_k)\right) \quad (3)$$

where the set of γ_k can be construed as prior weights on the point sets. The values of these weights are constrained such that $\gamma_k \geq 0$ and $\sum_{k=1}^K \gamma_k = 1$.

Segmentation protocols often yield multiple objects with each object corresponding to a unique label. Assuming a point set surface representation of those labeled objects, we denote the point subset of X_k corresponding to label l as $X_{k,l}$ and, similarly, the corresponding PDF as $P_{k,l}(X_{k,l})$. For inclusion of multi-label information (assuming L labels), we define the energy function to be minimized as the sum of the JHCT entropies for the L sets of K PDFs written as follows:

$$\mathrm{JHCT}_\alpha(\mathbf{P}_{1,1\ldots L}(X_{1,1\ldots L}),\ldots,\mathbf{P}_{K,1\ldots L}(X_{K,1\ldots L}),\boldsymbol{\gamma}) = \sum_{l=1}^L\left(H_\alpha\left(\sum_{k=1}^K \gamma_k\mathbf{P}_{k,l}(X_{k,l})\right) - \sum_{k=1}^K \gamma_k H_\alpha(\mathbf{P}_{k,l}(X_{k,l}))\right). \quad (4)$$

B. Properties of the $JHCT_\alpha$ Divergence

Several salient properties are associated with the HCT generalized entropy. Burbea and Rao demonstrate that the JHCT_α divergence is convex if and only if $\alpha \in [1,2]$ [19]. Additionally, the mutual information defined via the JS or JHCT_α divergences is not a distance metric due to their failure to satisfy the triangular inequality [19]. Nevertheless, extending that which is demonstrated in [24] with respect to the JS divergence, Majtey *et al.* show that the square root of the JHCT_α, $\alpha \in [1,2]$ is indeed a distance metric [25]. For a similarity measure, this is a desirable property that allows one to treat the measure with the usual intuitive notions of distance in Euclidean space.

Of equal importance is the α tuning parameter which characterizes the HCT entropy. By varying the α value between $[1,2]$ one can 'tune' the solution type between the ML estimate (*á la* [10]) at $\alpha = 1$ for a more sensitive measurement and the more noise robust L_2 estimate (*á la* [12]) at $\alpha = 2$. Sections III–VI are meant to illustrate this spectrum of solutions by providing several experimental evaluations where this feature is explored using our point set registration method in comparison with the algorithms of [12] and [10]. A good discussion of related topics is provided in [17].

C. Manifold Parzen Windowing for Geometrically-Based Density Estimation

The calculation of the JHCT divergence requires the transformation of each point set to its corresponding PDF. Each point set is represented as a PDF via a Gaussian mixture model (GMM). Assuming K point sets denoted by $\{X_k, k \in \{1,\ldots,K\}\}$, the kth point set is comprised of N_k points and is denoted by $\left\{x_1^k,\ldots,x_{N_k}^k\right\}$. The kth PDF is calculated from the kth point set as

$$\mathbf{P}_k(s) = \frac{1}{N_k}\sum_{i=1}^{N_k} G\left(s; x_i^k, C_i^k\right) \quad (5)$$

where $G\left(s; x_i^k, C_i^k\right)$ is a Gaussian with mean x_i^k and covariance C_i^k evaluated at s.

Whereas previous work used isotropic Gaussians [14], we use the local point set neighborhood to estimate an appropriate covariance matrix where the local structure of the point set is reflected in the anisotropy of that covariance using a technique called *manifold Parzen windowing* [26]. As described earlier, the point sets discussed in this work refer to point set surface representations derived, for example, from a segmentation

protocol. A traditional Parzen window representation of the manifold utilizes spherical Gaussians where the density of each Gaussian is isotropic in space regardless of the configuration of the manifold at that point. In contrast, the manifold Parzen windowing approach allows us to model the surface in a more accurate way by using a training set of surface points in the vicinity of an individual point. These training points are used to formulate the corresponding Gaussian density such that is oriented along the manifold which is a better reflection of the underlying structure. Further discussion in the context of classification is provided in [26] although the results and illustrations are equally applicable to this work.

For each point, x_i, the associated weighted covariance matrix, $C_{\mathcal{K}_i}$, is given by

$$C_{\mathcal{K}_i} = \frac{\sum\limits_{x_j \in \mathcal{N}_i, x_j \neq x_i} \mathcal{K}(x_i; x_j)(x_i - x_j)^T (x_i - x_j)}{\sum\limits_{x_j \in \mathcal{N}_i, x_j \neq x_i} \mathcal{K}(x_i; x_j)} \tag{6}$$

where $\mathcal{N}_i$ is the local neighborhood of the point x_i and $\mathcal{K}$ is a user-selected neighborhood weighting kernel. We use an isotropic Gaussian for $\mathcal{K}$ with variance $\sigma^2_{\mathcal{K}_i}$ as well as a k-d tree structure for efficient determination of $\mathcal{N}_i$ [27].

Calculation of the gradient requires the inverse of each covariance matrix. Determination of $C_{\mathcal{K}_i}$ from (6) could potentially result in an ill-conditioned matrix problematizing the calculation of the gradient. For this reason, we use the modified covariance [26]

$$C_i = C_{\mathcal{K}_i} + \sigma_n^2 I \tag{7}$$

where I is the identity matrix and σ_n is a parameter denoting added isotropic Gaussian noise. This particular aspect of our point set matching formulation will be explained in a later section as it is incorporated into a deterministic annealing strategy during optimization.

D. Calculation of the $JHCT_\alpha$ Divergence Measure and Gradient

Subsequent to calculation of the covariances, sample sets are generated for calculation of both the JHCT_α measure and its gradient. Both evaluations require the generation of a set of sample points from each of the K PDFs. These samples are generated by sampling n points from the distribution.

We designate the number of sample points generated for each of the K probability density functions as $\{M_1, \ldots, M_K\}$ and the kth set of points as $\left\{s_1^k, \ldots, s_{M_k}^k\right\}$. Equation (3) is then calculated using the sets of points and the formula

$$\begin{aligned}&\mathrm{JHCT}_\alpha(\mathbf{P}_1, \ldots, \mathbf{P}_K) \\ &= \frac{1}{1-\alpha}\left[\frac{1}{M}\left(\sum_{k=1}^{K}\sum_{j=1}^{M_k}\left[\mathbf{P}^*\left(s_j^k\right)\right]^{\alpha-1} - 1\right)\right. \\ &\qquad \left. - \frac{1}{N}\sum_{k=1}^{K}\frac{N_k}{M_k}\left(\sum_{j=1}^{M_k}\left[\mathbf{P}_k\left(s_j^k\right)\right]^{\alpha-1} - 1\right)\right]\end{aligned} \tag{8}$$

where

$$\mathbf{P}^*(X) = \frac{1}{N}\sum_{k=1}^{K}\sum_{i=1}^{N_k} G\left(x; x_i^k, C_i^k\right) \tag{9}$$

and

$$N = \sum_{k=1}^{K} N_k, M = \sum_{k=1}^{K} M_k. \tag{10}$$

The prior weighting values are calculated from $\gamma_k = N_k/N$ such that the larger point sets are weighted more heavily.

For many optimization routines the gradient with respect to the individual points is also required. This is calculated in a straightforward manner from (8)

$$\begin{aligned}&\frac{\partial \mathrm{JHCT}_\alpha}{\partial x_i^k} \\ &= -\frac{1}{M_k N}\sum_{j=1}^{M_k}\frac{G\left(s_j^k; x_i^k, C_i^k\right)\left(C_i^k\right)^{-1}\left(x_i^k - s_j^k\right)}{\left[\mathbf{P}_k(s_j^k\right]^{2-\alpha}} \\ &\quad + \frac{1}{MN}\sum_{k'=1}^{K}\sum_{j=1}^{M_{k'}}\frac{G\left(s_j^{k'}; x_i^k, C_i^k\right)\left(C_i^k\right)^{-1}\left(x_i^k - s_j^{k'}\right)}{\left[\mathbf{P}^*(s_j^{k'}\right]^{2-\alpha}}.\end{aligned} \tag{11}$$

III. Deformable Point Set Registration

The JHCT_α divergence measure introduced in the previous sections can be used as a correspondence measure within a point set registration framework. In this section we describe the remaining two components—the transformation model and the optimization strategy.

Associating each point set with a continuous mapping function, $\mathcal{T}_k$, and minimizing the JHCT_α divergence with respect to the parameters of all K transformation models brings the point sets into correspondence. Assuming the L parameters for the kth transformation model are denoted by the set $\left\{\phi_1^k, \ldots, \phi_L^k\right\}$, the derivative of the JHCT_α divergence with respect to the lth transformation parameter of the kth transformation model is given by

$$\frac{\partial \mathrm{JHCT}_\alpha}{\partial \phi_l^k} = \sum_{i=1}^{N_k}\frac{\partial \mathrm{JHCT}_\alpha}{\partial x_i^k}\frac{\partial \mathcal{T}_k}{\partial \phi_l^k} \tag{12}$$

where the term on the right is derived from the selected transformation model.

A. Directly Manipulated Free-Form Deformation

Given a transformation space, we attempt to find the optimal transformation, $\mathcal{T}^*$, corresponding to each point set which minimizes the JHCT divergence between the PDF's, i.e.,

$$\begin{aligned}\boldsymbol{\mathcal{T}}^* &= \mathcal{T}_1^*, \ldots, \mathcal{T}_K^* \\ &= \underset{\mathcal{T}_1, \ldots, \mathcal{T}_K}{\operatorname{argmin}}\{\mathrm{JHCT}_\alpha(\mathcal{T}_1(\mathbf{P}_1), \ldots, \mathcal{T}_K(\mathbf{P}_K))\}.\end{aligned} \tag{13}$$

For the fixed/moving point set pair scenario, we apply the transformation only to the moving point set and maintain the transformation corresponding to the fixed point at identity.

For n-D domains, we define the kth transformational model to be

$$\mathcal{T}_k(\phi_{i_1,\ldots,i_n}) = \sum_{i_1=1}^{M_1} \cdots \sum_{i_n=1}^{M_n} \phi_{i_1,\ldots,i_n} \prod_{j=1}^{n} B_{i_j,d_j}(u_j) \quad (14)$$

where $\phi_{i_1,\ldots,i_n}$ is an n-D grid of control points and $B_{i_j,d_j}(u_j)$ is the B-spline in the i_jth direction of order d_j. To find the control point values which define the minimizing transformation, we employ the following steepest descent iterative scheme:

$$\begin{aligned} \boldsymbol{\phi}^{i+1} &= \boldsymbol{\phi}^i + \lambda^i \nabla \mathrm{JHCT}_\alpha \left(\mathcal{T}_1(\mathbf{P}_1), \ldots, \mathcal{T}_K(\mathbf{P}_K)\right) \\ &= \boldsymbol{\phi}^i + \lambda^i \frac{\partial \mathrm{JHCT}_\alpha}{\partial \boldsymbol{\mathcal{T}}} \frac{\partial \boldsymbol{\mathcal{T}}}{\partial \boldsymbol{\phi}^i} \end{aligned} \quad (15)$$

where $\boldsymbol{\phi}^i$ is the set of control point values defining $\boldsymbol{\mathcal{T}} = \{\mathcal{T}_1, \ldots, \mathcal{T}_K\}$ and λ^i is the step size both taken at the ith iteration. Traditional gradient-based optimization approaches, which are intrinsically susceptible to hemstitching during the gradient ascent/descent, calculate $\partial \mathcal{T}_k / \partial \phi_l$ as

$$\frac{\partial \mathcal{T}_k}{\partial \phi_l} = \prod_{j=1}^{n} B_{l_j,d_j}(u_j). \quad (16)$$

In contrast, we calculate a preconditioned version of the gradient

$$\frac{\partial \mathcal{T}_k}{\partial \phi_l} = \frac{\prod_{j=1}^{n} B_{l_j,d_j}(u_j) \prod_{j=1}^{n} B^2_{l_j,d_j}(u_j)}{\sum_{k_1=1}^{d_1+1} \cdots \sum_{k_n=1}^{d_n+1} \prod_{j=1}^{n} B^2_{k_j,d_j}(u_j)} \cdot \left(\frac{1}{\sum_{\forall u_j} \prod_{j=1}^{n} B^2_{l_j,d_j}(u_j)} \right). \quad (17)$$

Additional details discussing the deficiency of traditional FFD gradient approaches as well as the derivation of (17) can be found in [28].

B. Deterministic Annealing

Minimization of the divergence measure occurs via gradient descent within a deterministic annealing framework [29], both in terms of the transformation model as well as the JHCT_α divergence, which decreases the susceptibility to local minima. At the initial stage of the optimization, the B-spline transformation model is defined by a low-resolution mesh to determine more global correspondence. At each subsequent level, the mesh-resolution is doubled [30] for increased local, refined registration. In coordination with this hierarchical registration, we specify an annealing schedule for the isotropic Gaussian noise discussed previously. At the pth iteration the covariance is calculated as

$$C_i = C_{\mathcal{K}_i} + \lambda^p \sigma_n^2 I \quad (18)$$

where λ is the annealing rate (typical values are in the range $[0.93, 1.0]$). This also has the effect of increasing the localization during the course of the optimization.

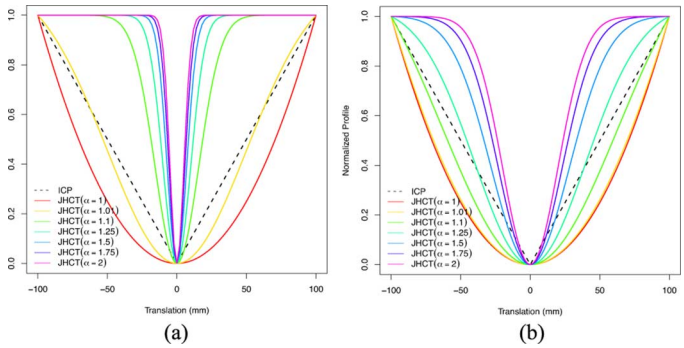

Fig. 1. JHCT profiles generated by translating a single point with no additive noise and different σ values: (a) $\sigma = 5$ mm and (b) $\sigma = 20$ mm. For reference, each of these plots has been created with the standard ICP metric which is represented by a dashed line. Note that the catchments widen with increasing σ and with decreasing α value where the illustrated α values are $\{1.0, 1.01, 1.1, 1.25, 1.5, 1.75, 2.0\}$.

IV. Open Source Implementation

The open source implementation of our point set registration methodology is currently available online [31]. Much of the basic functionality of our contribution and the code organization is based on the Insight Toolkit of the National Institutes of Health. Two principal components of our work derive from two previous contributions that we made to the open source community, specifically the JHCT divergence measure between two point sets [32] and a B-spline scattered data approximation algorithm [33], [34] used in our transformation model. As with all software in the Insight Toolkit our contribution includes source code, documentation, sample data, and automated testing through the CMake testing environment.

V. Experimental Evaluation

Several experimental evaluations were performed to illustrate the concepts mentioned in previous sections. We first evaluate the JHCT divergence in comparison with ICP[1] on sample point sets to demonstrate the effects of the α parameter. We then apply our point set registration framework to matching 2-D point sets derived from lung boundaries and comparing algorithmic performance with the algorithms of [10] and [12], and standard ICP combined with DMFFD. Finally, we demonstrate how the proposed algorithm performs on large 3-D multilabeled data sets derived from segmentations of pulmonary CT.

A. Evaluation of the Jensen–Havrda–Charvat–Tsallis Divergence

To demonstrate the flexibility afforded by the JHCT divergence, we show measurement profiles illustrating its catchment area, the extent of local minima, and the susceptibility to noise. In addition, for each set of profiles, we plot the corresponding ICP metric value for comparison. To provide an adequate context for the remainder of this subsection, we first generate profiles, given in Fig. 1, from the simple scenario of a single moving point measured against a single fixed point. The moving point was translated from 0 mm relative to the fixed point to a distance of 100 mm. Measurements were taken from -100 to 100

[1]We used a standard implementation provided in the Insight Toolkit.

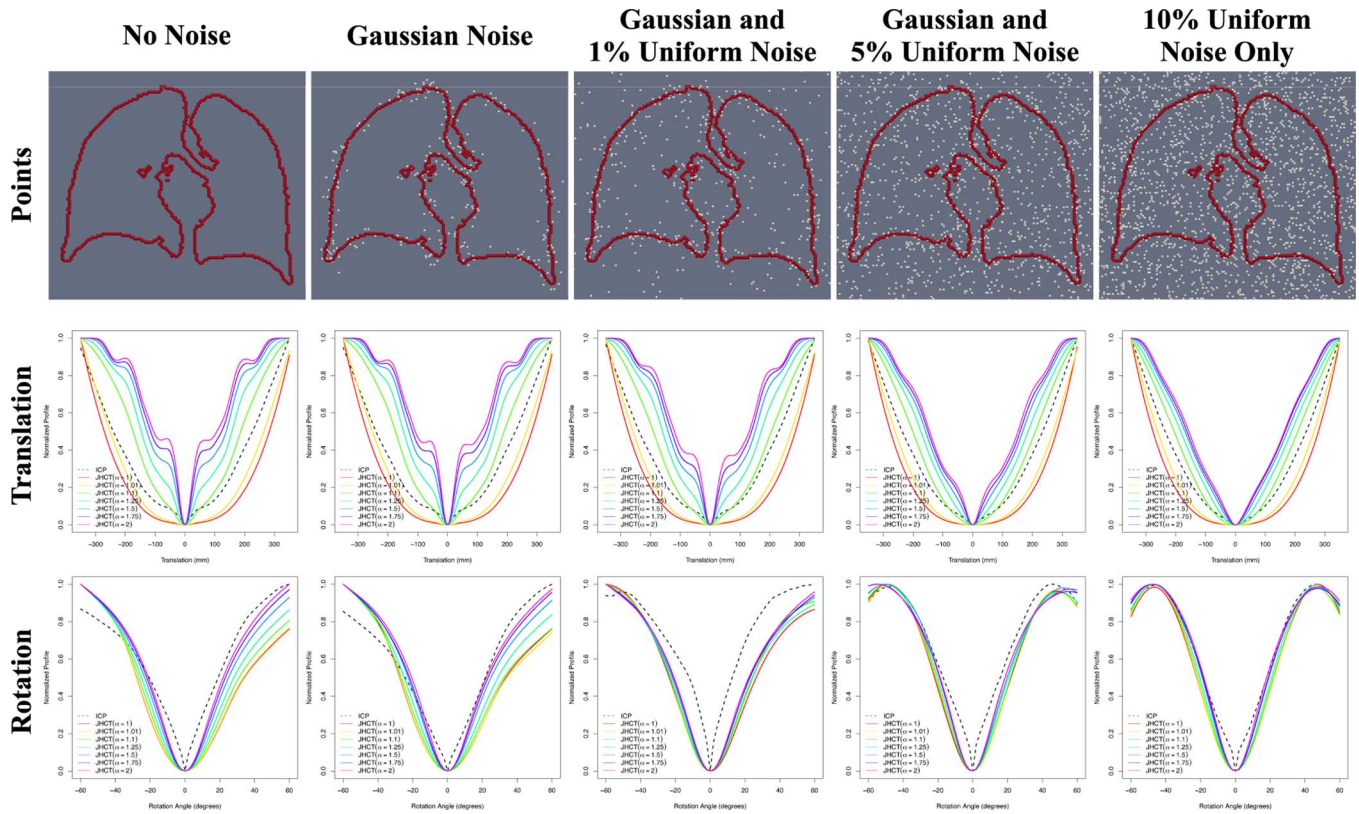

Fig. 2. Top row: Sample point set data derived from the segmentation of a coronal he-3 MRI which were used to create the profiles given in Fig. 2. Each of these four data are characterized by the type and amount of noise added to the noise-free point set in the first column: (second column) Gaussian noise only with a 5 mm standard deviation where the number of points was approximately half the number of total points in the noise-free point set, (third column) the same parameters as the second column but with additive uniform noise where 1% of voxels in the original he-3 MRI were converted to uniform noise outliers, (fourth column) Gaussian noise and 5% uniform noise, and (fifth column) only 10% uniform noise. Middle row: Profiles generated by translating the corresponding point sets between $[-350$ mm, 350 mm] in each column and varying the α parameter (ICP is represented by the dashed black line). Bottom row: Profiles generated by rotating the corresponding point sets around the center of mass of the true point set between $[-60°, 60°]$ in each column where $\alpha \in \{1.0, 1.01, 1.1, 1.25, 1.5, 1.75, 2.0\}$.

mm to provide the symmetric profiles which demonstrate that as α increases value from 1 to 2, the profiles narrow. We also see that increasing σ has a similar effect which increases the capture range, as is expected.

Similar measurements and corresponding profiles were derived from 2-D point sets extracted from axial lung boundaries. 15 pairs of 3-D helium-3 MRI of the lungs were acquired before and after respiratory challenge (exercise or methacholine induced). Axial MRI data were acquired on a 1.5 T whole body MRI scanner (Siemens Sonata, Siemens Medical Solutions, Malvern, PA) with broadband capabilities and a flexible ^{3}He chest radiofrequency coil (IGC Medical Advances, Milwaukee, WI; or Clinical MR Solutions, Brookfield, WI). During a 10–20 s breath hold following the inhalation of approximately 300 mL of hyperpolarized ^{3}He mixed with approximately 700 mL of nitrogen a set of 19–28 contiguous axial sections were collected. Parameters of the fast low angle shot sequence for ^{3}He MR imaging were as follows: repetition time msec/echo time msec, 7/3; flip angle, 10°; matrix, 80 × 128; field of view, 26 cm × 42 cm; section thickness, 10 mm; and intersection gap, none. Following acquisition of the hyperpolarized helium-3 MR data, the data was de-identified prior to analysis. In-plane resolution was approximately 3.2 mm × 3.2 mm.

The boundary of each set of lungs was segmented and 2-D mid-axial or mid-coronal lung boundaries were converted into point sets where each voxel on the boundary was converted to a point. We only used one of the inspiratory lung pairs in this particular section although all 15 lung pairs were used in the experiments detailed in Section IV.

In addition to comparing the different α values, we investigated a couple different noise models. Specifically, we illustrate how the different α values influence the similarity measure in the presence of additive random Gaussian and uniform noise. Similar to the single point profiles, we include the ICP similarity measure for comparison. The coronal lung boundary point sets used to produce the similarity profiles in Figs. 2 and 3 are illustrated in the first row of Fig. 2 where the original point set and the additive noise is rendered in red and white, respectively.

Since varying the σ value tends to only widen the catchment area (as shown in Fig. 1) we maintain $\sigma = 20$ mm for all the derived profiles in this section. For each experiment involving randomly generated noise, each measurement along the x-axis was performed 10 times with different generated noise and the average value was plotted. Whereas the number of Gaussian noise points was held constant at approximately half the number of points of the original point set with a standard deviation of 20 mm, the amount of uniform noise varied from 1% of voxels in the original helium-3 MRI, which were converted to uniform noise outliers, to 10% of the image voxels.

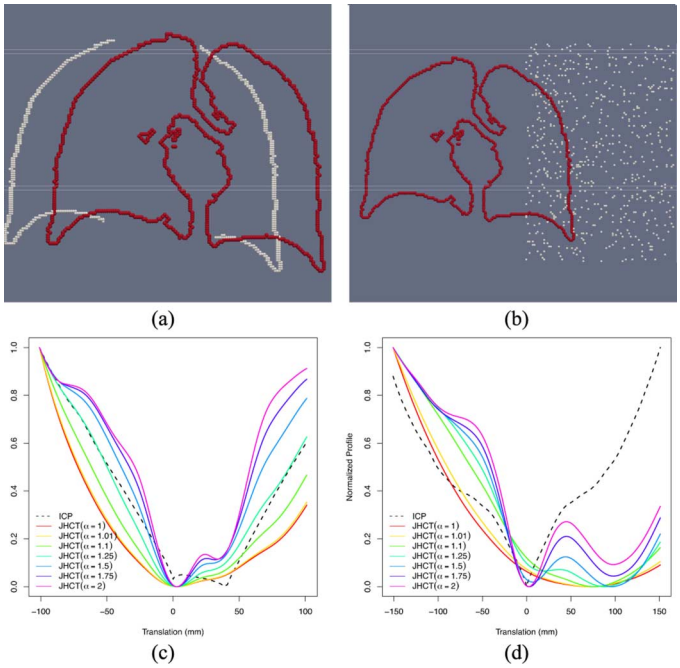

Fig. 3. (a) Outlier point set derived from the original lung coronal image concatenated with a shifted (40 mm in the positive x direction), incomplete copy of itself. The corresponding profiles in (b) were created by translating the point set in the x direction from -100 to 100 mm where the original lung coronal boundary point set is situated at the origin (ICP is represented by the dashed black line). Due to interpolation error, the number of boundary points in the incomplete shifted copy were doubled in certain spots which caused the ICP global minimum to shift to $x = 40$ mm. However, the robust JHCT measure at $\alpha = 2$ has a well-defined narrow valley close to the true minimum and that the valley broadens as $\alpha \rightarrow 1$. (b) Second outlier point set where 5% uniform noise was confined to a subregion of the original image. This causes the global minimum of the JHCT family of similarity profiles to shift although the values closer to $\alpha = 1$ get shifted more than the values close to $\alpha = 2$. In contrast the global minimum for the ICP metric remains at the origin.

The translation profiles associated with the no-noise case in the first column of Fig. 2 illustrate a very broad valley for α values close to 1 (similar to the ICP profile) which progressively narrow as $\alpha \rightarrow 2$. Additional local minima are present for these larger α values due to, for example, the alignment of the left and right lungs (consistent with discussion in [17]) which persist despite additional Gaussian noise (second column of Fig. 2). These local minima disappear as uniform noise is added which is a rather unlikely scenario encountered in actual application. Regardless of additive random noise type, though, profiles corresponding to α values closer to 2 are more narrow than those closer to 1.

For the profiles in Fig. 2, it was implicitly assumed that the noise has been centered on the true point set. However, that is not necessarily always the case and in Fig. 3 we provide two different examples which illustrate additional properties of the JHCT similarity measure and a comparison with the ICP metric. In Fig. 3(a) we construct a point set which is composed of the original coronal lung boundary points rendered in red and a shifted $(\Delta x = 40$ mm$)$, incomplete copy of itself rendered in white. Due to interpolation issues, some portions of the shifted lung boundary doubled in the number of points. The profiles were created by translating this corrupted point set relative to the fixed point set composed of the original lung boundary points. This resulted in the profiles seen in Fig. 3(c). It is interesting to note, first, that the ICP global minimum has shifted from the origin to the location of the shifted, incomplete copy whereas the JHCT measures all maintain global minima at the origin although local minima at the shifted location are seen for α values closer to 2.

This is in contrast to the scenario depicted in Fig. 3(b) which was created by confining 5% uniform noise to a subregion located on the right side of the image and the original lung boundary is translated with respect to the corrupted image. Here, the ICP metric manifests its global minima at the origin unlike the shifted global minima depicted by the profiles associated with α values closer to 1. Although local minima are present at this shifted location for α values closer to 2, the global minima are shifted much closer to the origin. In this way, the JHCT divergence for α values closer to 2 behave like the statistical median as opposed to α values closer to 1 which are more analogous to the statistical mean [17]. The JHCT divergence provides a simple tuning mechanism to alter behavior in the presence of different types of noise.

B. Comparative Evaluation of Kernel-Based Methods on Real Data

As a continuation of the last section, we explore the effects of varying the α parameter on actual data. This data, described previously, consisted of 15 pairs of helium-3 MRI lung image volumes acquired either coronally or sagitally before and after respiratory challenge. Depending on the acquisition orientation, either a mid-axial or mid-coronal slice was extracted from each image volume. In plane resolution varied from 1.6×1.6 mm^2 to 3.3×3.3 mm^2. Since each boundary point of the segmentation was converted to a 2-D point set, the in-plane resolution provides a sense of the range in spacing between neighboring points. Each point set was comprised of ~ 1000 points. Since mid-volume slices might not necessarily correspond exactly between acquisition times or since gas may or may not be present in the trachea, some features present in one point set might not be present in its counterpart. We view this experimental feature as representative of possible outliers one might encounter in likely applications and investigate the performance of our proposed methodology with this in mind.

As an ancillary investigation, we compare our method with other kernel-based point set registration strategies. Specifically, we use the open source implementation of the algorithm described in [12] recently implemented by one of the authors who has made the source code available online.[2] The author also coded the algorithm discussed in [10] within the same framework for easy comparison. This helps to ensure the quality of the implementation of previously published routines for comparison with our method. An additional comparison is made by incorporating the ICP similarity metric into our proposed algorithmic framework using slightly modified ITK classes. Thus, the transformation of the ICP-based algorithm is modeled using the DMFFD transformation/regularization method discussed in a previous section. Furthermore, we modified our code to ensure that certain common parameters between the algorithms

[2]http://code.google.com/p/gmmreg/

had identical meaning such as the σ parameter governing the Gaussian kernel size in constructing the GMM.

For each registration, a similarity transform (scale and translation) was calculated from both point sets to warp the moving point set into the space of the fixed point set. Translation and scale values were calculated from the centroids and Frobenius norms of the two point sets, respectively. This initial transformation was identical for all four algorithms (where we count the JHCT family of algorithms as one) such that differences in performance are strictly attributed to the deformable registration component. For the deformable registration, four levels were used with a maximum of 100 iterations at each level. The σ values for the four levels were $\sigma = \{2.0, 1.0, 0.5, 0.25\}$ and no explicit regularization on the thin-plate spline transformation, i.e., $\lambda = 0$ for all four levels. These values were similar to the default values provided in the open source offering of these two other algorithms where the sigma values were normalized and scaled to the square root of the Frobenius norm of the fixed point set.

A few differences should be noted. First, these two other algorithms use thin-plate splines to model the deformation instead of *B*-splines. In terms of capabilities, most of the point sets derived from CT lung data used in a later experimental section consist of approximately 10^5 points each with our implementation capable of handling larger point sets. In contrast, the capabilities of the previously specified available software for these other methods are much more limited in that the maximum number of points accommodated is at least a couple of orders of magnitude less (e.g., point set sizes used in [12] is limited to less than 200 points each with only a theoretical discussion of sizes exceeding 300 points). In addition, these other routines do not accommodate labeled point sets (which would be obtained from such image analysis tasks as multi-label image segmentation). This motivates the rather limited point set data used in this experimental section.

To compare the performance between algorithms and algorithmic variants, we calculated the average directed distance, δ, between the fixed point set, X, and the warped point set, Y, such that δ is defined to be

$$\delta(X,Y) = \frac{\vec{d}(X,Y) + \vec{d}(Y,X)}{2} \tag{19}$$

where $\vec{d}(X,Y)$ is the directed distance from X to Y. This directed distance is defined as

$$\vec{d}(X,Y) = \frac{1}{|X|} \sum_{x \in X} \min_{y \in Y} \|x - y\|. \tag{20}$$

The results of the 15 point set pairs$\times$ 10 algorithms $=$ 150 registrations are illustrated in Fig. 4. Although all registration algorithms performed well (as attested by the median average directed distance), the JHCT algorithms for $\alpha \in \{1, 1.01, 1.1, 1.25\}$ performed better than the other six sets of results which were all sub-pixel resolution.[3] The best performer, in terms of the median average directed distance, was the JHCT algorithm for $\alpha = 1.1$. This points out the possible importance of being able to tune the α parameter for optimal performance between the ML estimate and more robust L_2 measure.

[3]Median values are roughly significantly different at the 95% confidence level if the notches do not overlap [35].

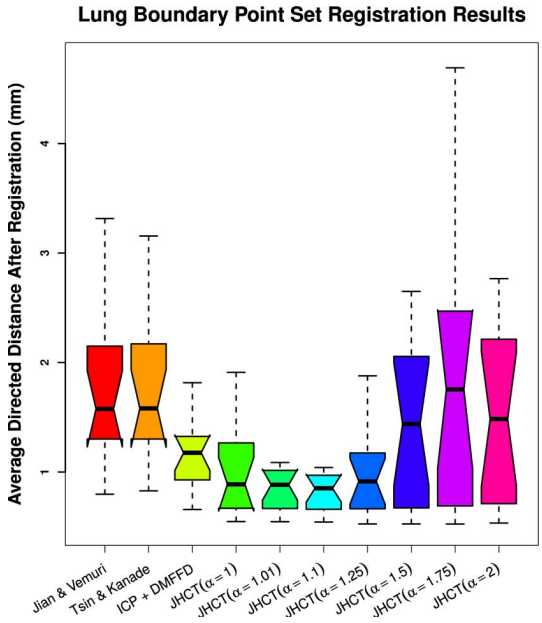

Fig. 4. Results of point set registration of the 15 pairs of helium-3 lung MRI. Several α values, $\alpha \in \{1, 1.01, 1.1, 1.25, 1.5, 1.75, 2.0\}$, were used in registering each of the 15 pairs. Also included in this assessment are the algorithms of Jian and Vemuri [12], Tsin and Kanade [10], and standard ICP [1] combined with the DMFFD transformation model [28].

Computation times (in seconds) to run the different algorithmic implementations for the different point set pairs which were comprised of different quantities of points is shown in Fig. 5 where the algorithms of [12] and [10] do slightly better than our algorithm in terms of absolute time for total point set quantities of < 1000. However, computation times increase rapidly for the other two kernel-based algorithms for quantities > 1000. These larger points sets were created by adding correlated noise.

The shape of the plots are best understood by realizing that the dominant portion of all three algorithms is the estimation of the gradient and similarity measure at each iteration. Since we use a kd-tree structure in our algorithm for quickly identifying neighboring points, the computational complexity is dominated by the time necessary to construct the kd-tree at each iteration which is known to be $O(n \log n)$ [27]. In contrast, the implementations of the other two algorithms written by the first author of [12] do not use any such speed-ups although [12] contains a discussion of potential speed-ups using a Gaussian transform.

C. Anatomically-Based CT Lung Registration

The motivating aim of this research is anatomically-based registration for CT lung kinematic and morphometry studies. Although success has been derived from applying intensity-based registration techniques to this problem [36]–[38], given the wealth of segmentation techniques that have been developed specifically for CT lung imagery (e.g., whole lungs, fissures, blood vessels, small and large airways), anatomically-driven registration is possible using our labeled point set

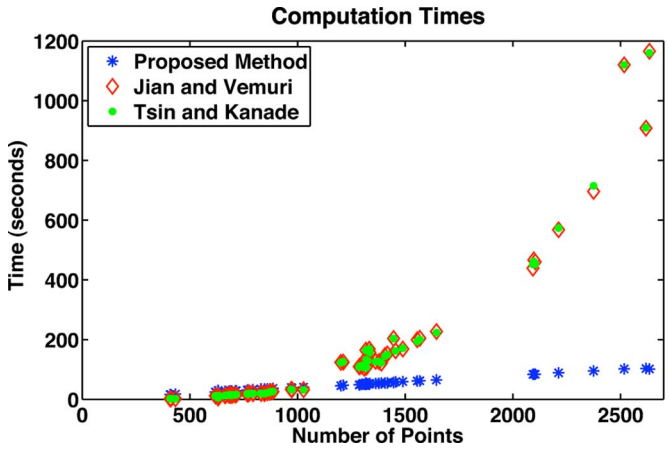

Fig. 5. Computation times (in seconds) for all three registration algorithms for the 68 registration pairs using the overall best parameter set for each algorithm. The quantity of points in the 68 registration pairs varied from ~ 400 to ~ 2700.

registration algorithm where each labeled point subset is used to represent specific anatomy.

The work presented in [39] and [40] describes an evaluation framework for CT lung image registration involving 10 data sets described as follows:

> Patient identifiers were removed in accordance with an institutional review board approved retrospective study protocol (RCR 03–0800). Each patient underwent treatment planning in which 4-D CT images of the entire thorax and upper abdomen were acquired at 2.5 mm slice spacing with a General Electric Discovery ST PET/CT scanner (GE Medical Systems, Waukesha, WI).

Whereas the first five image sets were cropped to include the entire rib cage and subsequently sub-sampled in plane to 256×256 voxels, the second set of five image data were left in their original in plane resolution of 512×512 voxels. Final in-plane voxel dimensions ranged from (0.97×0.97) to (1.16×1.16) mm^2 with each case exhibiting a slice thickness of 2.5 mm.

A thoracic imaging expert manually delineated five image pairs using a Matlab-based GUI created specifically for this purpose. Manual demarcation of points was facilitated by generating a local neighborhood window over which is calculated the normalized cross correlation to identify corresponding features. After the initial landmark identification by the primary reader, two secondary readers re-identified the points. The primary reader also re-identified the landmarks. These 10 data sets have been made publicly available[4] and were used in this section to show the capabilities of our proposed method in comparison with our modified deformable ICP algorithm.

For each of the 7 image data inspiratory/expiratory pairs (due to technical issues, we only used 7 of the 10 image data) we segmented the left and right lungs using the technique developed in [41]. A segmentation of the blood vessels in both lungs was then obtained using the technique described in [42] where the pruning/smoothing stage was omitted to create realistic noise/outliers potentially encountered in actual application. The inspiratory point sets are registered to their expiratory counterparts (which are kept fixed). These registrations were computed using α values from the set $\{1.0, 1.01, 1.1, 1.25, 1.5, 1.75, 2.0\}$.

The point set registration was performed in two stages. During the first stage, only a small fraction the surface points of both the left and right lungs were used to bring the lung surfaces into alignment (typical point set sizes employed during this registration step consisted of 10 000–20 000 points for each lung). The results from this more global alignment stage were then used as the initialization of a more refined registration step in which the points from the vessel tree were combined with the lung boundary points to drive the registration. Each of the left and right vessel trees consisted of approximately 75 000–150 000 points. The parameters of these two registration steps were as follows.

1) Global Registration.
   - *B*-spline order: cubic.
   - Number of levels: 1.
   - Number of control points: $5 \times 5 \times 4$.
   - Maximum number of iterations: 100.
   - $\sigma_n = 4.0$ [see (7)].
   - $\lambda^2 = 0.93$ [see (18)].
2) Local Registration
   - *B*-spline order: cubic
   - Number of levels: 3.
   - Level 1
     — number of control points: $11 \times 11 \times 7$;
     — maximum number of iterations: 20;
     — $\sigma_n = 2.0$ [see (7)].
   - Level 2
     — number of control points: $19 \times 19 \times 11$;
     — maximum number of iterations: 10;
     — $\sigma_n = 1.0$ [see (7)].
   - Level 3
     — number of control points: $35 \times 35 \times 19$;
     — maximum number of iterations: 5;
     — $\sigma_n = 0.5$ [see (7)].
   - $\sigma_{\mathcal{K}_i} = 5.0$ [see (6)].
   - $\mathcal{N}_{\mathcal{K}_i} = 5$ [see (6)].
   - $\lambda^2 = 0.93$ [see (18)].

Note that the σ values are based on normalization to the point set, as described earlier, using the square root of the Frobenius norm of the fixed point set. The reader should also be aware that this experimental setup was not meant to be optimal in terms of absolute registration results with respect to this data set. It was merely meant for comparative purposes between the family of JHCT algorithmic variants and the deformable ICP algorithm.

Registration accuracy was inferred by average landmark error of the 300 landmarks, the selection process detailed earlier. It should be noted that although the landmarks correspond within each inspiratory/expiratory pair, they do not necessarily correspond across data sets. The landmark analysis results are summarized in Fig. 6.

Landmark error improved for all 7 point set pairs for all registrations during the global registration step which is probably due to the minimal noise in the first registration component produced by the lung segmentation algorithm [41]. However, the well-known susceptibility of the ICP metric to outliers (see, for example, [2]) and the presence of such outliers in the second

[4]http://www.dir-lab.com

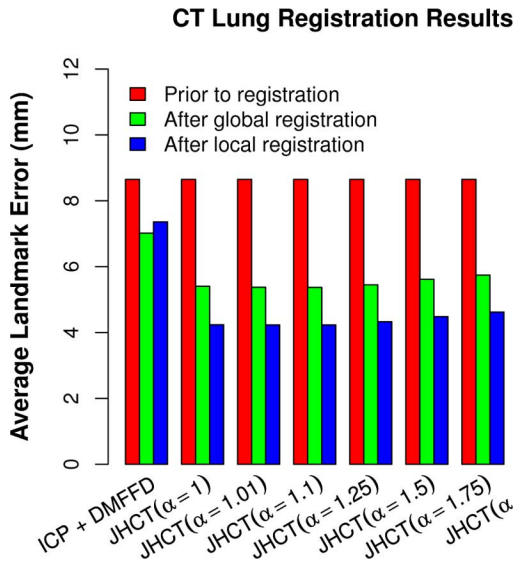

Fig. 6. Results from anatomic feature-based CT inspiratory/expiratory lung registration across 7 image pairs using the different algorithmic configurations listed in the figure. Note the improvement in average landmark error ($n = 300$ landmarks) for each algorithm at the end of the global registration stage. However, most likely due to the amount of noise present in the local point sets, the ICP landmark error is slightly worse after the local registration step. Although the JHCT family of algorithms performed similarly for these data, α values closer to 1 showed a slight improvement over values closer to 2.

step of the registration process provides a possible explanation for the increase of landmark errors seen in the ICP results following registration. In contrast, results obtained using different α values were very similar after both registration steps with a trend showing slightly better results for α values closer to 1.

VI. Discussion and Conclusion

Geometric feature analysis via point set correspondence assessment is important for many medical image analysis tasks. The work presented in this paper contributes to the growing number of algorithms already published in the literature. A generalization of the Jensen-Shannon divergence, known as the Jensen–Havrda–Charvat–Tsallis divergence, was used to measure the similarity between spatial configurations of labeled point sets. To accommodate the local structure of many extracted point sets, we incorporated Manifold Parzen windowing into the actual point set divergence measure for a more accurate representation of the features of interest. We have also presented this point set measure in conjunction with a relatively novel transformation/regularization model based on *B*-splines known as directly manipulated free form deformation. This DMFFD transformation model takes advantage of many of the salient properties of *B*-splines without the problematic energy topographies associated with the traditional FFD transformation model.

Several experiments were performed to showcase the various components of our contribution. Metric profiles with varying alpha and sigma values in the presence of different noise models were provided in various experimental evaluations to showcase the flexibility of our method. This is important given the various potential applications for which this work might prove useful. We also provided a performance comparison of our algorithm with the algorithms of [10] and [12] where it was demonstrated that our algorithm, overall, performed favorably relative to these other kernel methods. One of the practical considerations raised from the experimental results was the utility of robust statistical measures used in other algorithms. Such robustness is potentially useful in the presence of certain type of outliers although these types of outliers would most likely not be present in typical applications. Regardless of the outlier type, the results illustrated from the JHCT α experiments motivates the use of not just the ML estimate nor the robust L_2 measure but a tuning to the specific application.

In addition there are several aspects of this work of practical significance which is often omitted or not considered in previous work. First, the algorithmic implementation was based on the Insight Toolkit and provided to the research community complete with technical documentation and testing. Thus, others can use the approach reported in this paper for their own applications or for comparison with other algorithms. Also, we have extended our algorithm to accommodate multilabeled point sets which is very useful for certain applications (e.g., [43]). This is an important consideration as many applications derive multilabel segmentations from images which are then used to drive the registration. For example, in the lung, there are several algorithms which independently segment the whole lung, vasculature, airway tree, lobar fissures, etc. Including this information into a point set registration should improve registration results over simply using a single label for all points.

We have also implemented the components of our approach into the more generalized suite of open source registration tools known as ANTS (Advanced Normalization Tools).[5] Components of this software toolkit have demonstrated competitive performance in intensity-based registration scenarios [28], [44]. The inclusion of the work described in this paper into ANTS allows for registration configurations not investigated in this work but could potentially be explored in future work. For example, one can combine the JHCT divergence measure with intensity-based registration (e.g., cross correlation) using the diffeomorphic Symmetric Normalization (SyN) transformation model [45] for labeled image data. One can also adopt an adaptive strategy where the similarity metric is varied during the optimization.

Acknowledgment

The authors would like to thank Dr. E. E. de Lange and Dr. T. A. Altes at the University of Virginia for providing the hyperpolarized image data.

References

[1] P. J. Besl and N. D. McKay, "A method for registration of 3-D shapes," *IEEE Trans. Pattern Anal. Mach. Intell.*, vol. 14, no. 2, pp. 239–256, Feb. 1992.

[2] S. Rusinkiewicz and M. Levoy, "Efficient variants of the ICP algorithms," in *Proc. 3rd Int. Conf. 3D Digital Imag. Model.*, Quebec City, Canada, 2001, p. 145.

[3] Z. Zhang, "Iterative point matching for registration of free-form curves and surfaces," *Int. J. Comput. Vis.*, vol. 13, pp. 119–152, 1994.

[4] A. Rangarajan, H. Chui, and F. L. Bookstein, "The softassign procrustes matching algorithms," in *Proc. Inf. Process. Med. Imag.*, 1997, pp. 29–42.

[5] http://www.picsl.upenn.edu/ANTS

[5] S. Gold, A. Rangarajan, C.-P. Lu, S. Pappu, and E. Mjolsness, "New algorithms for 2D and 3D point matching: Pose estimation and correspondence," *Pattern Recognit.*, vol. 31, no. 8, pp. 1019–1031, 1998.

[6] H. Chui and A. Rangarajan, "A new point matching algorithm for non-rigid registration," *Comput. Vis. Image Understand.*, vol. 89, pp. 114–141, 2003.

[7] F. L. Bookstein, "Principal warps: Thin-plate splines and the decomposition of deformations," *IEEE Trans. Pattern Anal. Mach. Intell.*, vol. 11, no. 6, pp. 567–585, 1989.

[8] K. Rohr, H. S. Stiehl, R. Sprengel, T. M. Buzug, J. Weese, and M. H. Kuhn, "Landmark-based elastic registration using approximating thin-plate splines," *IEEE Trans. Med. Imag.*, vol. 20, no. 6, pp. 526–534, Jun. 2001.

[9] S. C. Joshi and M. I. Miller, "Landmark matching via large deformation diffeomorphisms," *IEEE Trans. Image Process.*, vol. 9, no. 8, pp. 1357–1370, Aug. 2000.

[10] Y. Tsin and T. Kanade, "A correlation based approach for robust point-set registration," in *Proc. Eur. Conf. Comput. Vis.*, 2004, pp. 558–569.

[11] M. Singh, H. Arora, and N. Ahuja, "Robust registration and tracking using kernel density correlation," in *Proc. IEEE Comput. Vis. Pattern Recognit. Workshop*, 2004, pp. 174–182.

[12] B. Jian and B. Vemuri, "A robust algorithm for point set registration using mixture of Gaussians," in *Proc. Int. Conf. Comput. Vis.*, 2005, pp. 1246–1251.

[13] H. Guo, A. Rangarajan, and S. Joshi, *Handbook of Mathematical Models in Computer Vision*. New York: Springer, 2005, ch. Diffeomorphic Point Matching, pp. 205–220.

[14] F. Wang, B. Vemuri, A. Rangarajan, and S. Eisenschenk, "Simultaneous nonrigid registration of multiple point sets and atlas construction," *IEEE Trans. Pattern Anal. Mach. Intell.*, vol. 30, no. 11, pp. 2011–2022, Nov. 2008.

[15] F. Wang, B. Vemuri, and T. Syeda-Mahmood, "Generalized L2- divergence and its application to shape alignment," *Inf. Process. Med. Imag.*, vol. 21, pp. 227–238, 2009.

[16] A. Basu, I. Harris, N. Hjort, and M. Jones, "Robust and efficient estimation by minimizing a density power divergence," *Biometrika*, vol. 85, pp. 549–559, 1998.

[17] D. W. Scott, "Parametric statistical modeling by minimum integrated square error," *Technometrics*, vol. 43, no. 3, pp. 274–285, 2001.

[18] N. J. Tustison, S. P. Awate, G. Song, T. S. Cook, and J. C. Gee, "A new information-theoretic measure to control the robustness-sensitivity trade-off for dmffd point-set registration," in *Proc. 21st Biennial Int. Conf. Inf. Process. Med. Imag.*, Williamsburg, VA, 2009, pp. 215–226.

[19] J. Burbea and C. R. Rao, "On the convexity of some divergence measures on entropy functions," *IEEE Trans. Inf. Theory*, vol. 28, pp. 489–495, 1982.

[20] P. Papoulis and S. U. Pillai, *Probabilty, Random Variables, and Stochastic Processes*. New York: McGraw-Hill, 2001.

[21] M. Havrda and F. Charvat, "Quantification method of classification processes: concept of structural alpha-entropy," *Kybernetica*, vol. 3, pp. 30–35, 1967.

[22] C. Tsallis, "Possible generalization of Boltzmann-Gibbs statistics," *J. Stat. Phys.*, vol. 52, pp. 479–487, 1988.

[23] M. Gell-Mann and C. Tsallis, *Nonextensive Entropy*. New York: Oxford Univ. Press, 2004.

[24] D. Endres and J. Schindelin, "A new metric for probability distributions," *IEEE Trans. Inf. Theory*, vol. 49, pp. 1858–1860, 2003.

[25] A. Majtey, P. Lamberti, and A. Plastino, "A monoparametric family of metrics for statistical mechanics," *Physica A*, vol. 344, pp. 547–553, 2004.

[26] P. Vincent and Y. Bengio, "Manifold parzen windows," in *Advances in Neural Information Prcessing Systems*, S. Thrun, S. Becker, and K. Obermayer, Eds. Cambridge, MA: MIT Press, 2003, pp. 825–832.

[27] M. de Berg, M. van Kreveld, M. Overmars, and O. Scharzkopf, *Computational Geometry: Algorithms and Applications*. New York: Springer, 2000.

[28] N. J. Tustison, B. B. Avants, and J. C. Gee, "Directly manipulated free-form deformation image registration," *IEEE Trans. Image Process.*, vol. 18, no. 3, pp. 624–635, Mar. 2009.

[29] K. Rose, "Deterministic annealing for clustering, compression, classification, regression, and related optimization problems," *Proc. IEEE*, vol. 86, no. 11, pp. 2210–2239, Nov. 2000.

[30] S. Lee, G. Wolberg, and S. Y. Shin, "Scattered data interpolation with multilevel B-splines," *IEEE Trans. Visualizat. Computer Graphics*, vol. 3, pp. 228–244, Jul./Sep. 1997.

[31] N. J. Tustison, S. P. Awate, and J. C. Gee, "Information-theoretic directly manipulated free-form deformation labeled point-set registration," *Insight J.*, pp. 1–10, 2009.

[32] N. J. Tustison, S. P. Awate, and J. C. Gee, "A novel information-theoretic point-set measure based on the Jensen–Havrda–Charvat–Tsallis divergence," *Insight J.*, pp. 1–6, 2008.

[33] N. J. Tustison and J. C. Gee, "Generalized n-d C^k B-spline scattered data approximation with confidence values," in *Proc. 3rd Int. Workshop Medical Imag. Augmented Reality*, 2006, pp. 76–83.

[34] N. J. Tustison and J. C. Gee, "N-d C^k B-spline scattered data approximation," *Insight J.*, pp. 1–10, 2005.

[35] R. McGill, J. W. Tukey, and W. A. Larsen, "Variations of box plots," *Am. Stat.*, vol. 32, no. 1, pp. 12–16, 1978.

[36] B. Li, G. E. Christensen, J. Dill, E. A. Hoffman, and J. M. Reinhardt, "3-D inter-subject warping and registration of pulmonary CT images for a human lung models," in *Proc. SPIE: Med. Imag.*, 2002.

[37] T. A. Sundaram and J. C. Gee, "Towards a model of lung biomechanics: Pulmonary kinematics via registration of serial lung images," *Med. Image Anal.*, vol. 9, no. 6, pp. 524–537, Dec. 2005.

[38] T. S. Cook, N. Tustison, J. Biederer, R. Tetzlaff, and J. Gee, "How do registration parameters affect quantitation of lung kinematics?," in *Med. Image Comput. Comput. Assist Interv. Int. Conf. Med. Image Comput. Comput. Assist. Interv*, 2007, vol. 10, pp. 817–824.

[39] R. Castillo, E. Castillo, R. Guerra, V. E. Johnson, T. McPhail, A. K. Garg, and T. Guerrero, "A framework for evaluation of deformable image registration spatial accuracy using large landmark point sets," *Phys. Med. Biol.*, vol. 54, no. 7, pp. 1849–1870, Apr. 2009.

[40] E. Castillo, R. Castillo, J. Martinez, M. Shenoy, and T. Guerrero, "Four-dimensional deformable image registration using trajectory modeling," *Phys. Med. Biol.*, vol. 55, no. 1, pp. 305–327, Jan. 2010.

[41] S. Hu, E. A. Hoffman, and J. M. Reinhardt, "Automatic lung segmentation for accurate quantitation of volumetric X-ray CT images," *IEEE Trans. Med. Imag.*, vol. 20, no. 6, pp. 490–498, Jun. 2001.

[42] G. Song, A. Ramirez-Manzanares, and J. C. Gee, "A simultaneous segmentation and regularization framework for vessel extraction in CT images," in *Proc. 1st Int. Workshop Pulmonary Image Anal. MICCAI 2008*, New York, 2008, pp. 185–194.

[43] N. J. Tustison, S. P. Awate, J. Cai, T. A. Altes, G. W. Miller, E. E. de Lange, J. P. Mugler, and J. C. Gee, "Pulmonary kinematics from tagged hyperpolarized helium-3 MRI," *J. Magn. Reson. Imag.*, vol. 31, no. 5, pp. 1236–1241, May 2010.

[44] A. Klein, J. Andersson, B. A. Ardekani, J. Ashburner, B. Avants, M.-C. Chiang, G. E. Christensen, L. D. Collins, J. Gee, P. Hellier, J. H. Song, M. Jenkinson, C. Lepage, D. Rueckert, P. Thompson, T. Vercauteren, R. P. Woods, J. J. Mann, and R. V. Parsey, "Evaluation of 14 nonlinear deformation algorithms applied to human brain mri registration," in *Neuroimage*, Jan. 2009 [Online]. Available: http://dx.doi.org/10.1016/j.neuroimage.2008.12.037

[45] B. B. Avants, C. L. Epstein, M. Grossman, and J. C. Gee, "Symmetric diffeomorphic image registration with cross-correlation: evaluating automated labeling of elderly and neurodegenerative brain," *Med Image Anal.*, vol. 12, no. 1, pp. 26–41, Feb. 2008.